Real-time pixel based early apple bruise detection using short wave infrared hyperspectral imaging in combination with calibration and glare correction techniques

Janos C. Keresztes[*], Mohammad Goodarzi, Wouter Saeys

KU Leuven, Department of Biosystems, MeBioS, Kasteelpark Arenberg 30, 3001 Leuven, Belgium

ABSTRACT

High speed data processing for online food quality inspection using hyperspectral imaging (HSI) is challenging as over hundred spectral images have to be analyzed simultaneously. In this study, a real-time pixel based early apple bruise detection system based on HSI in the shortwave infrared (SWIR) range has been developed. This systems consists of a novel, homogeneous SWIR illumination unit and a line scan camera. The system performance was tested on Jonagold apples bruised less than two hours before scanning. Partial least squares-discriminant analysis was used to discriminate bruised pixel spectra from sound pixel spectra. As the glossiness of many fruit and vegetables limits the accuracy in the detection of defects, several reflectance calibrations and pre-processing techniques were compared for glare correction and maximizing the signal to noise ratio. With the best combination of first derivative and mean centering, followed by image post-processing, this system was able to detect fresh bruises in thirty apples with 98% accuracy at the pixel level with a processing time per apple below 200 ms.

© 2016 Elsevier Ltd. All rights reserved.

1. Introduction

Over 80 million tons of apples are produced worldwide every year, with a production growth of 3.10% and a yield growth of 2.31% (FAOSTAT, 2016). Bruising is one of the most important causes of commercial loss in the apple industry. Bruises usually occur by impact damage during harvest, transportation, cleaning or on the sorting line (Van Zeebroeck et al., 2007). In the bruised regions, the damaged cells release their content in the apple matrix such that polyphenol is exposed to oxygen, resulting in browning of the tissue. This is not appreciated by consumers (Soliva-Fortuny, Grigelmo-Miguel, Odriozola-Serrano, Gorinstein, & Mart'in-Belloso, 2001). Traditionally, bruised apples are identified through visual inspection and removed manually, which is a laborious task. Therefore, there is a demand for machine vision technology for rapid and non-destructive, early bruise detection in apples.

Machine vision technology is already widely used in the apple industry for on-line sorting automation (Blasco, Aleixos, & Moltó, 2003; Cubero, Aleixos, Moltó, Gómez-Sanchis, & Blasco, 2011). However, this technology fails to effectively detect bruises in several apple varieties with detection accuracies as low as 63% (Soliva-Fortuny et al., 2001). Moreover, small or fresh bruises often remain undetected as the spectral signatures of healthy and bruised regions in the visible range (400–700 nm) are very similar shortly after bruising when the oxidative browning is still limited (Kleynen, Leemans, & Destain, 2005). Furthermore, the stalk or calyx of apples should not face the imager (Wenqian Huang, Chi Zhang, Jiangbo Li, Liping Chen, & Chunjiang Zhao, 2012), because these

---

are often interpreted as bruises by the computer vision systems (Wen & Tao, 1999). Therefore, a setup for apple orientation on a sorting line has been developed to avoid the presence of stalk or calyx in image by orienting the apples with 97.7% accuracy for 14 different cultivars (Unay et al., 2011). While such a system reduces the number of false positives by avoiding erroneous classification of the stalk or calyx as bruises, it limits bruise detection to the zones around the equator of the fruit. So, bruises on the top and bottom side of the fruit will not be detected by this system.

In order to build a robust apple sorting system which can detect small defects while handling different cultivars, several setups have been proposed using multispectral and hyperspectral imaging (HSI) in the Visible and Near Infrared (Vis-NIR) range (Kleynen et al., 2005; Unay et al., 2011). Using Vis-NIR HSI for model building has been shown to lead to a better detection of bruises in different apple varieties such as Golden Delicious, Jonagold and Braeburn (Ariana & Lu, 2010), as well as other types of food (ElMasry, Wang, Vigneault, Qiao, & ElSayed, 2008; Esquerre, Gowen, O'Donnell, & Downey, 2009; Lin et al., 2003). Since different cultivars have different spectral signatures, a sorting line which can handle multiple cultivars would be very valuable. Moreover, the large number of spectral variables per pixel and the large number of pixels per fruit makes real-time pixel classification based on the full spectrum challenging from a computational point of view. In addition, the lack of clear spectral differences in the visible and very near infrared range (400–1000 nm) between sound and recently bruised tissue gave rather low detection accuracies for fresh bruises (Kavdir & Guyer, 2005; Mehl, Chao, Kim, & Chen, 2002). While promising results for early bruise detection in apples have been reported for Short Wave Infrared (1000–2500 nm SWIR) HSI (Baranowski, Mazurek, Wozniak, & Majewska, 2012; Horabik, Baranowski, & Tys, 2007; Kim et al., 2011), and online Vis-NIR HSI has been demonstrated for industrial applications (Bae, Kim, Kim, & Lee, 2006; Wu et al., 2012), robust industrial SWIR HSI on fruit and vegetables remains challenging. It has also been reported that vis-NIR bruise detection is more challenging in bi-colored apples (Van Zeebroeck et al., 2007). Therefore, the aim of this study was to investigate the potential of SWIR HSI for real-time bruise detection in Jonagold apples, the most important bi-colored apple cultivar in Flanders (VLAM, 2015).

Compared to the Si based sensors used in the 400–1000 nm range, the Indium Gallium Arsenide (InGaAs) and Mercury Cadmium Tellurium (MCT) based focal plane array (FPA) sensors used in SWIR imagers are more sensitive to manufacturing defects, temperature variation and cooling fluctuations, which result in pixel to pixel non uniformity (Parra, Meza, & Torres, 2014). Researchers have investigated non-uniformity compensation (Isoz, Svensson, Renhorn, Box, & Linköping, 2005) for infrared imagers in defense and security applications (Battaglia, Burzi, Moyer, Sudol,

& Passe, 2010), involving reference measurements on a large reflectance standard covering the entire field of view. However, the sub-region reflectance calibration methods typically used in food sorting applications using SWIR HSI do not correct for such spatial and spectral non-uniformity as those panels are expensive.

Common broadband illumination within SWIR hyperspectral imaging systems use Halogen spots (Baranowskiet al., 2012; Feng & Sun, 2012; Kim et al., 2011; Xing, Symons, Hatcher, & Shahin, 2011). Those spots are placed empirically around the field of view, not considering the curvature of the samples, thus resulting in limited uniformity. The combination of this poor illumination uniformity with the glossiness of the waxy skin of fruit and vegetables limits the detection accuracy for damaged regions (Huang, Zhang, Li, & Zhang, 2013).

To overcome the above mentioned limitations for SWIR HSI, the added value of optimal homogeneous illumination, pixel based reflectance calibration and glare correction techniques has been investigated in this study. The added value of those techniques is compared on a case study of online early apple bruise detection.

## 2. Materials and methods

2.1. Apple samples

Thirty Jonagold apples were purchased at a Belgian local supermarket. The apples were first kept at room temperature for 24 h, then imaged before and 2 h after damage. The apples were weighted using a scale (Adventurer Pro, Ohaus, Nänikon, Switzerland). The radius of curvature was measured prior to bruising using a depth gage measurement device (digimatic depth gage 543, Mitutoyo, Chicago, USA), in combination with the following formula (Mohsenin, 1984):

$$R_{x,y} = \frac{(AC)^2}{8(BD)} + \frac{(BD)}{2} \tag{1}$$

where the parameters are defined as illustrated in Fig. 1.

The depth gage with $AC = 19.13$ mm, was first calibrated on a flat surface such that when the points A, B and C are aligned, with B centered between A and C, the device measures $BD = 0.00$ mm. The depth gage was then placed on the spot where the apple will be damaged and the depth BD was measured along the meridional (stem-calyx) and equatorial planes of the apple. The derived radii r_x, r_y using (1) were averaged using the harmonic average (Zarifneshat, S. Ghassemzadeh et al., 2010):

$$R = \frac{2r_x r_y}{r_x + r_y} \tag{2}$$
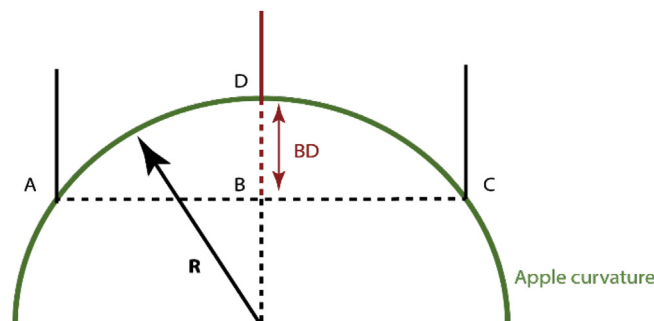
Fig. 1. Radius of curvature measurement. The device consists of two fixed points A and C and one variable point D along the BD axis. When placed on the surface of an apple, the radius of curvature R can be deduced from the distance AC between the two fixed points and the relative distance BD away from the AC segment.

The apples were bruised using the pendulum device described by Van Zeebroeck et al. (Van Zeebroeck et al., 2003). An electromagnet was used to trigger the impacts consistently. The displacement was measured with an angular encoder placed on the rotational axis of the pendulum. A dynamic force sensor (D1051V3, Dytran Instruments, Chatsworth California, USA) placed on the hemi-spherical impactor of 25 mm diameter was used to monitor the impact forces. The apples were bruised on the equator with an impact energy of 0.41 ± 0.01 J, or an equivalent peak force of 76.79 ± 6.86 N.

2.2. Hyperspectral imaging

2.2.1. Sample illumination

Illumination of food sorting systems is often poorly described in literature or not designed for the targeted application. As proper illumination is crucial for accurate results (Feng & Sun, 2012; Kim et al., 2011; Nicolaï et al., 2007), different design steps and setups were evaluated in this work. Four 20 W DC tungsten halogen spots (Decostar 51 ALU, Osram, Munich, Germany) were placed in an arc configuration around a spherical object representing an apple, using the spherical coordinates form (r, θ, φ) with r the distance away from the arc center, θ the polar angle between the projection in the conveyor plane of the spot and the scanning direction x and φ the azimuthal angle locating the spot's vector position away from z, the normal to the conveyor. The spots 1, 3, 2, and 4 are respectively located at $(r_{arc}, \pm \alpha_{1arc}, 90°)$, $(r_{arc}, \pm \alpha_{1arc}, 90°)$ and $(r_{arc}, \pm \alpha_{1arc}, 90°)$ with a radii $r_{arc} \in [300mm-600 mm]$, and angles α_{1arc} and $\alpha_{2arc} \in [5°-85°]$ with the constraint $\alpha_{1arc}-\alpha_{2\ arc}<8°$. Two extra spots were placed in an arc attached perpendicularly to the aforementioned arc with spherical coordinates $(r, \pm \alpha, 0°)$ with $r \in [300 mm-600 mm]$ and $\alpha \in [5°-55°]$. The origin was the center of a hemisphere representing an apple, of radius 75 mm. The X axis represent the direction of scanning, the Y axis the width of the sample, and the Z axis the height of the sample, as seen in Fig. 2a. The design was then modeled considering its angular and spectral distribution in ray tracing software (TracePro 7.4, Lambda research, Littleton, Massachusetts, USA). The merit function was the coefficient of variability (CV), being the ratio between the standard deviation and the mean of a normalized 1D irradiance line. To consider the curvature in X-Z and Y-Z planes, the average between

CV_{XZ} and CV_{YZ} was considered, being CV_{mean}. These profiles are both situated on the center of a spherical object, as depicted in Fig. 2b. The positioning of the spots was optimized to minimize CV_{mean}, or equivalently to maximize uniformity. The Down Hill Simplex algorithm available in TracePro was used at multiple starting points during optimization. The resulting configuration and uniformity can be observed in Fig. 2a. Diffusers with high transmittance in the SWIR range (DGP5011, Knight Optical, Kent, UK) were mounted on each spot to increase the uniformity. As the SWIR HSI is a line scanner, only a line of 0.5 mm wide has to be illuminated uniform. For the ease of interpretation, let us consider the normalized irradiance distribution of the illuminated hemisphere, observed in Fig. 2b. The % of uniformity can be defined as $(1 - CV) \cdot 100\%$. The center of the hemisphere has maximal irradiance. Observing Fig. 2b and c, the scanned region has 15% of deviation, giving a CV_{YZ}=0.172, or a uniformity of 82.7%. Similarly, a uniformity of 77.79% is obtained for the vertical profile. Thus, an averaged uniformity of 80.28% is obtained on the overall hemisphere. As apples are acquired using a line scanner observing the drawn region of interest (ROI), only the horizontal irradiance profile with angles above 5° from the horizontal matters, which corresponds in this case to 30 mm away from the center. The resulting ROI is up to 85% uniform. For more details on the illumination design the reader is referred to (Keresztes, De Ketelaere, Audenaert, Koshel, & Saeys, 2015).

2.2.2. Hyperspectral imaging system

An infrared HgCdTe camera (xeva 2.5—320, Xenics, Leuven, Belgium) with a bith depth of 14 bits was mounted on a spectrograph (SWIR hyperspec, Headwall Photonics, Massachusetts, USA) using a slit of 60 μm and a SWIR lens (Oles22.5, Specim, Oulu, Finland). This imager was mounted 400 mm above a conveyor belt (custom model, ITRA, Belgium), as illustrated in Fig. 3. Retroreflective proximity sensors (model CY-192B-P-Y-C, Panasonic Electric Works, Osaka, Japan) were mounted on each end of the conveyor belt to trigger the start and stop line scan acquisition and prevent the apples from falling off the belt at the end. The spectral imager was designed to acquire 200 spectral bands ranging from 900 to 2500 nm with a pixel-to-pixel spectral resolution of 7.34 nm, and 320 pixels along the scanning line of pixel resolution 1.7 mm. The conveyor speed was set to 0.1 m/s, while the imager acquired

(a)   (b)   (c)
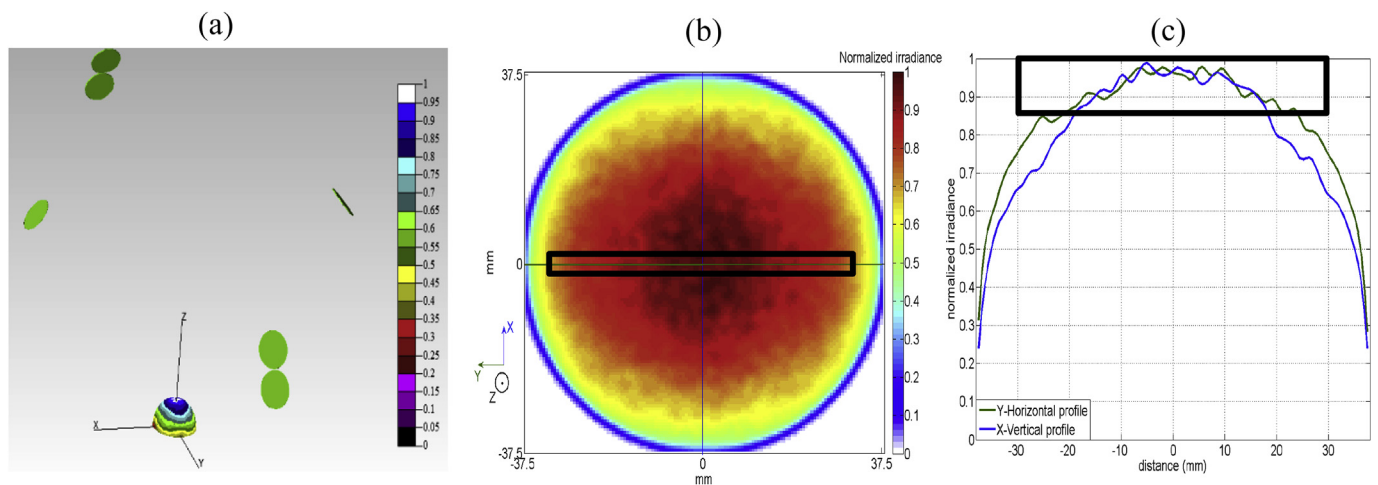
Fig. 2. a) 3D normalized irradiance on a half sphere of 6 spots optimally positioned at r_{arc} = 589 mm, r = 412 mm, and angles α_{1arc} = ±58.43°, α_{2arc} = ±63.50°, and α = ±42.43°, b) corresponding irradiance profiles on the half sphere surface, c) linear irradiance profiles in the horizontal (blue) and vertical (green) direction with respect to the center of the half sphere surface. The effective ROI of the HSI has been marked with a black rectangle. (For interpretation of the references to color in this figure legend, the reader is referred to the web version of this article.)
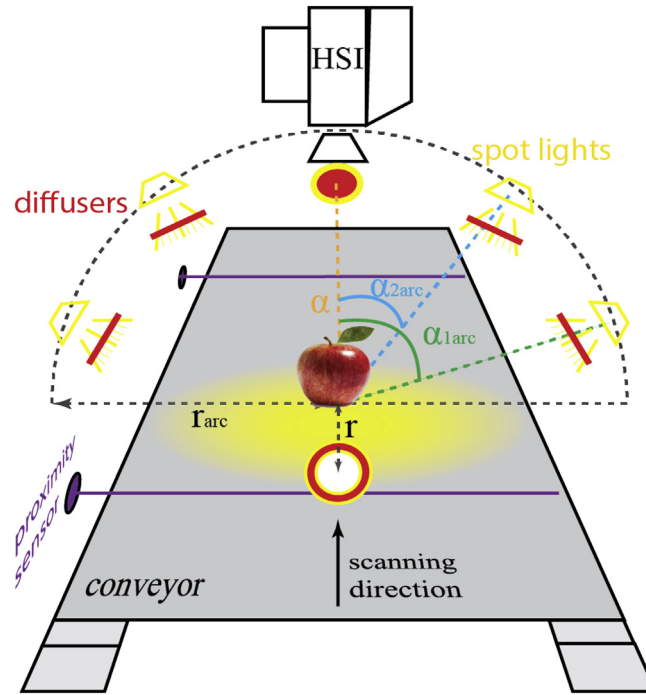
Fig. 3. Schematic representation of the setup for hyperspectral imaging of apples using 6 optimally positioned halogen spots (yellow) with diffusers (red). The imager is triggered by proximity sensors (purple). (For interpretation of the references to color in this figure legend, the reader is referred to the web version of this article.)

60 lines per second, thus providing a spatial resolution of 0.5 mm per line. The overall setup including the illumination was enclosed in a black tunnel consisting of low SWIR reflectivity clothing (100% black wool, Pauli, Leuven, Belgium) attached onto a frame. The hyperspectral imaging setup was controlled using Labview 2012 in combination with a frame grabber PXI-1428 to ensure high speed data acquisition and processing (both National instruments, Austin, TX).

2.2.3. Multivariate data analysis

During the offline model building phase, the hyperspectral images were processed in Matlab 2014a (The Mathworks, Natick, MA, USA) for reflectance calibration, region of interest extraction and hypercube unfolding. Multivariate data analysis was then performed on the unfolded matrices of pixel spectra using the PLS toolbox 7.8 (Eigenvector research Inc, Wenatchee, WA). The final calibration model was exported to Labview using the Model Exporter 2.5 (Eigenvector research Inc, Wenatchee, WA) for real-time bruise detection in apples. A flowchart of the processing steps is presented in Fig. 4.

2.2.4. Reflectance calibration

The dark current $D(x,\lambda)$ at each position x on the line and each wavelength λ was measured 30 min after sensor cooling stabilization, by placing an opaque cap in front of the lens. A Spectralon panel consisting of a 99% reflectance standard of 50×300 mm (Labsphere, North Sutton, Hampshire, USA) was used as a lambertian spectral reference. For this panel, the absolute reflectance spectrum $R_{panel}(\lambda)$ in the wavelength range 400—2500 nm was provided by the vendor (Laser2000, The Nederlands) with 1 nm resolution. Based on the available reference information, the following three reflectance calibrations $R_i(x,\lambda)$ were proposed:

$$R_1(x, \lambda) = \frac{I_{Raw}(x, \lambda) - D(x, \lambda)}{Ref_1(\lambda) - D(x, \lambda)} \tag{3}$$

$$R_2(x, \lambda) = \frac{I_{Raw}(x, \lambda) - D(x, \lambda)}{Ref_2(x, \lambda) - D(x, \lambda)} \tag{4}$$

$$R_3(x, \lambda) = \frac{I_{Raw}(x, \lambda) - D(x, \lambda)}{Ref_2(x, \lambda) - D(x, \lambda)} \cdot R_{panel}(\lambda) \tag{5}$$

Where $I_{Raw}(x,\lambda)$ is the acquired raw irradiance intensity for the sample expressed in digital numbers (DN), $Ref_1(\lambda)$ is the 99% reference intensity at wavelength λ in DN averaged over the entire panel, $Ref_2(x,\lambda)$ is the 99% reference intensity at wavelength λ in DN acquired at the xth pixel. The reference and dark current measurements were averaged over 50 and 500 acquired lines, respectively, every 30 min to correct for the effects of temporal variability of the sensor. The calibration methods $R_1(x,\lambda)$, $R_2(x,\lambda)$ and $R_3(x,\lambda)$ will further on be referred to as the reference pixel method (RPM), the pixel based reflectance (PBR) and pixel based with absolute reflectance correction (PBARC), respectively.

2.2.5. Spatial and spectral region of interest

As the contrast between the mean spectra for apples and background was the largest at 1082 nm, this image was used to automatically segment the images. All pixels for which the reflectance at 1082 nm exceeded the threshold of 35% were labeled as apple pixels, while the others were labeled as background. In a second step, holes were filled inside the mask using image morphology. For each pixel segmented as apple, the reflectance spectra were calculated using Equations (3)—(5). The data above 2100 nm and below 1000 nm were discarded as no spectral signatures were observed for sound nonglossy and bruised apple tissues above 2100 nm, and a low signal to noise ratio (SNR) was observed below 1000 nm. In order to reduce the dimension of the dataset
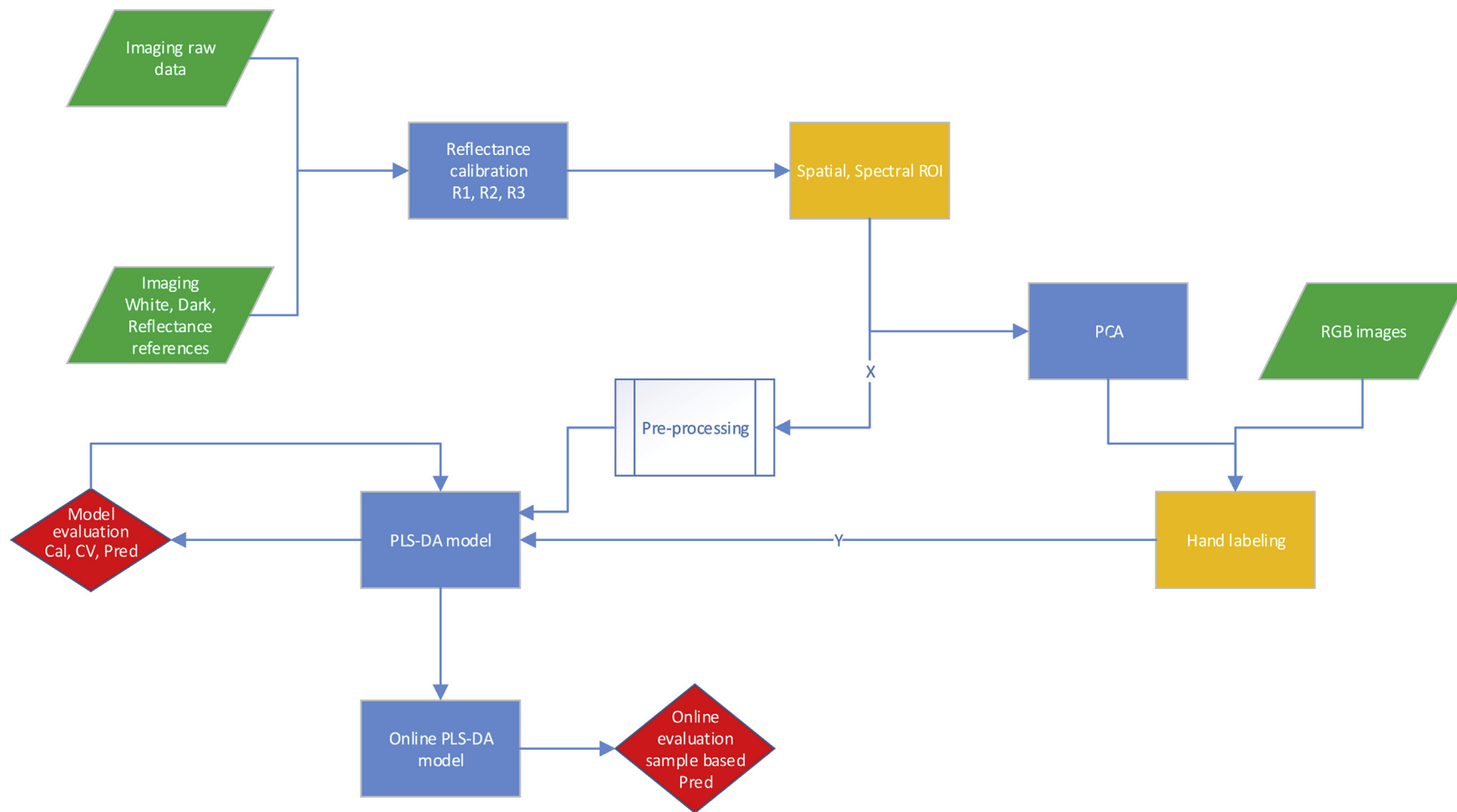
Fig. 4. Data handling flowchart. The acquired images (reference, samples and ground truth), data processing (reflectance calibrations, model building), user-interactions (region of interest selection, reference images labeling) and evaluation are respectively indicated in green, blue, yellow and red. (For interpretation of the references to color in this figure legend, the reader is referred to the web version of this article.)

prior to bruise detection, only the pixels included in the mask were used to unfold the relevant data points of the 3D hyperspectral cube into a 2 dimensional matrix of pixel spectra **X**. The spatial information for each pixel in the mask was preserved during the unfolding process to allow refolding after the multivariate data analysis.

2.2.6. Spectral pre-processing

As variation in the acquired intensities due to fruit curvature and light scattering effects can negatively affect the reliability of the multivariate models, the pixel spectra were pre-processed prior to model building (Barbin, Elmasry, Sun, & Allen, 2012). In the context of apple bruise detection, most of the unwanted scattering regions are due to glare. The following, commonly used, empirical pre-processing techniques were tested (Curcio & Petty, 1951; Goodarzi, Sharma, Ramon, & Saeys, 2015): normalization, mean centering, first and second derivatives, Multiplicative Scatter Correction (MSC) and Standard Normal Variate (SNV). The spectra were first normalized by dividing each spectrum by maximum value. This preprocessing was motivated by the observation that the glossy regions on the apples had a higher reflectance in the 1000–1800 nm range. By normalizing each spectrum by dividing all reflectance values by the maximum value, the glossy and non-glossy regions would have the same range of reflectance values in the 1000–1800 nm range. Mean centering involves subtraction of the mean value over all pixel spectra for each spectral variable. The first derivative removes additive scatter effects, while the second derivative also removes multiplicative scatter effects. The derivatives were computed using the Savitzky-Golay method using a second order polynomial and 9 and 15 window points empirically selected for the first and second derivative, respectively. SNV calculates the mean and standard deviation over all wavelengths of an individual pixel spectrum and standardizes each variable in the spectrum by subtracting this spectrum-specific mean value and dividing by this spectrum-specific standard deviation. MSC corrects for additive and multiplicative scattering by estimating a, b coefficients by projecting the measured spectrum onto a reference spectrum, being here the mean. The different pre-processing techniques were tested individually and combined with posterior mean centering, as summarized in Table 4.

2.2.7. Image reference measurements

After bruising and data acquisition, the apples were kept at room temperature for one week. Pictures of the bruises were then taken after peeling, as illustrated in Fig. 5b. As it was not possible to perfectly align the RGB images of the peeled apples with acquisition of the hypercubes, manual labeling of the bruised regions in the hypercubes was required. After applying the image mask and unfolding the hyperspectral cube, a principal component analysis (PCA) was applied to the dataset without any pre-processing. The scores of the three first principal components capturing respectively 98.36%, 1.24% and 0.15% of the variance were each normalized to represent color values. A virtual RGB image was created from these hypercubes by assigning the red, green and blue color to the first, second and third components, respectively. By each time placing the RGB image of the peeled apple next to the virtual RGB image of the same apple, the sound, bruised and glossy regions in the hypercube could be labeled, as illustrated in Fig. 5c. This labeling was guided by peeled bruised apple images using the LabelMe toolbox (Russell, Torralba, Murphy, & Freeman, 2008), followed by human inspection to correct for orientation or illumination changes. The glossy regions were assigned with 20% of brightness change from the specular reflection regions. It should be noted here that the Jonagold PCA-RGB score images presented in Fig. 5a are very similar to the PCA scores images reported in literature (Horabik et al., 2007). The number of region pixels per apple was reduced by 50% by thresholding a random uniformly distributed pattern overlapping the glare, bruise and apple masks to reduce the redundancy in the training set and speed up the model building. This percentage was selected empirically. From the 15
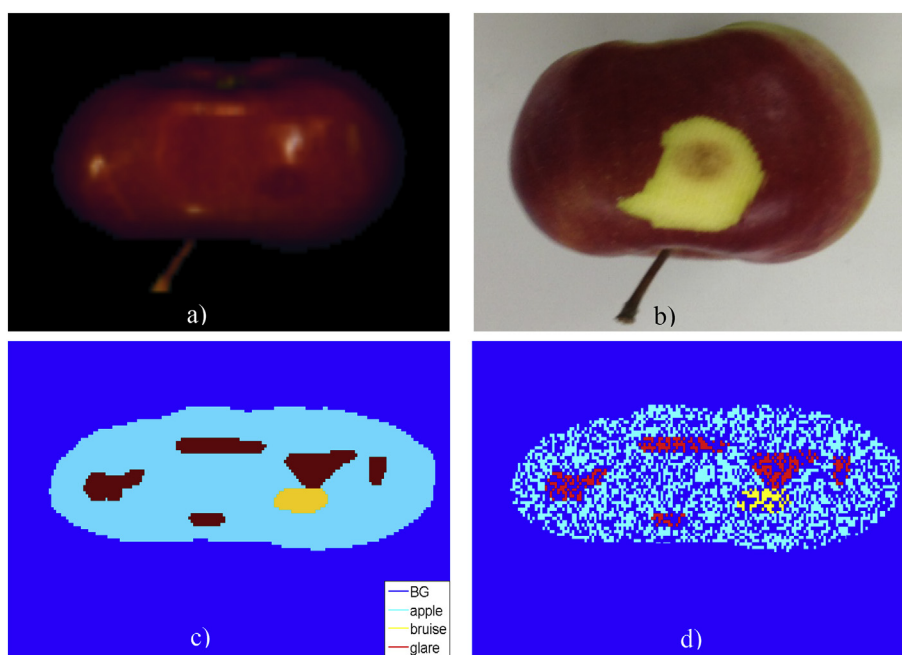
Fig. 5. a) Virtual Red, Green, Blue (RGB) image representing respectively the first, second and third PC scores for the SWIR hypercube of a Jonagold apple 2 h after bruising, b) RGB image for the same, slightly differently oriented, apple, peeled 1 week after bruising c) PCA RGB image manually labeled to indicate the apple (cyan), glare (red), bruise (yellow) and background (blue) pixels, d) sampled pixels for model building. (For interpretation of the references to color in this figure legend, the reader is referred to the web version of this article.)

labeled apples, using the data reduction, a total of 14,769, 6173 and 7245 pixels corresponding to the apple (healthy region), bruise and glare classes respectively were selected to build the multivariate classification models. The effect of this random reduction of the number of pixels in the training set is illustrated in Fig. 5d. Fifteen other apples were prepared in the same fashion to build a prediction dataset. To cover all the imaged pixels, each apple was individually loaded at full-resolution, and classification metrics were derived. The metrics for each apple were then averaged.

2.2.8. Bruise pixel classification

As Partial Least Squares Discriminant Analysis (PLS-DA) has been shown in previous studies to be a powerful technique for hyperspectral data analysis (Feng & Sun, 2012), it was used to build a two-class classifier to distinguish bruised and sound pixels, and a three-class classifier to distinguish bruised, glare and sound apple tissue pixels. From the labeled regions described above, the glare was considered as sound apple regions when using a binary classifier. To evaluate the number of needed latent variables (LVs), cross validation was performed using venetian blinds on 30% of the calibration set with 15 data splits. This approach enabled to capture most of the variability between pixels with a limited number of apples, for both calibration and cross-validation. The remaining 15 apples were used as a test set.

The usefulness of all combinations of the different reflectance calibration methods and pre-processing techniques for binary and ternary PLS-DA classification was evaluated using the root mean square error of calibration, cross-validation and prediction (RMSEC, RMSECV, RMSEP), sensitivity, specificity and classification accuracy. For each combination of pre-processing method and classification model, the RMSEC and RMSECV values were plotted as a function of the number of latent variables and the optimal number of LVs was selected empirically at the first local RMSECV minimum. The prediction model was then applied to the same apples one by one to observe the RMSEP, and adapt the number of LVs to prevent over or under-fitting. The specificity, sensitivity and accuracy are summarized per calibration method for the bruise class for only the best performing combinations. The root mean squared errors and other metrics were calculated as follows:

$$RMS = \sqrt{\frac{\sum_{i=1}^{N}(\widehat{y}_i - y_i)^2}{N}} \qquad (6)$$

$$Sensitivity = \frac{TP}{(TP + FN)} \qquad (7)$$

$$Specificity = \frac{TN}{(FP + TN)} \qquad (8)$$

$$Accuracy = \frac{TP + TN}{T + N} \times 100\% \qquad (9)$$

Where in (6), $\widehat{y}_i - y_i = 0$ if the pixel is correctly classified, and 1 otherwise, N represents the number of pixels compared. In formulae (6–9), TP, TN, FP, FN, T, N indicate respectively the numbers of true positives, true negatives, false positives, false negatives, positives and negatives. For best performance, the RMS should be minimal, while the sensitivity and specificity should be close to 1, and the accuracy should be close to 100%.

2.2.9. Bruise volume measurement

No clear visible bruise was noticed until 36 h after bruising. So, the bruise volume measurement was performed one week after bruising to make sure that the bruise had fully developed. The bruise surface and depth were measured using a caliper (Digimatic caliper 500, Mitutoyo, Chicago, USA) by first peeling off the skin, and further slicing the apple perpendicularly to the bruise surface. The following formula was used to derive the bruise volume (Bollen, Nguyen, & Dela Rue, 1999):

$$V = \frac{\pi(d_b - d_t)}{24}\left(3w_1 w_2 + 4(d_b - d_t)^2\right) \qquad (10)$$

where w_1 and w_2 are the small and large diameter of the bruise surface and d_b-d_t the relative depth of the bruise, as observed in Fig. 6.

2.2.10. Wavelength selection

In order to better understand why PLS-DA performs best when a separate class is assigned for glare, a reverse interval PLS-DA wavelength selection has been applied for the binary and ternary classifiers with their best performing preprocessing technique, selecting 10 consecutive bands of 73 nm total spectral bandwidth (Goodarzi & Saeys, 2016; Serranti, Cesare, & Bonifazi, 2013). The iteration stops if the removal of any additional band increases the misclassification rate, or similarly decreases the accuracy.

2.2.11. Image post-processing

It is recommended to use image post processing to improve the prediction accuracy (Baranowski et al., 2012). As we are interested in small but significant bruise areas, those above 17 mm² are considered in this work (Pang, Studman, Banks, & Baas, 1996). Therefore, a particle filter was applied to remove clusters of pixels classified as bruised of less than 20 pixels. This filter was applied to pixel-based 2 and 3 class PLS-DA classification with the best performing reflectance calibration method, using all the wavelengths.

2.2.12. Real-time validation

From the prediction accuracy results, the best performing model using the best performing reflectance calibration was exported to
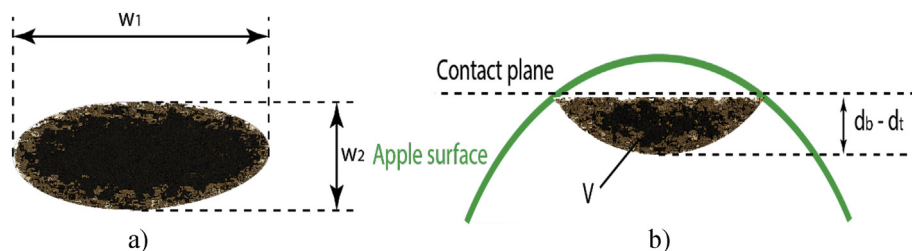
Fig. 6. a) surface and b) depth apple bruise measurement. After impact, the bruise region starts at the contact plane and spreads into the apple. The bruise volume is denoted as V. The bruise depth is denoted as d_b-d_t, while the small and large bruise diameter at the contact plane cross-section are denoted as w_1 and w_2, respectively.

Labview using the Model Exporter 2.5 (Eigenvector research Inc, Wenatchee, USA). This prediction model was then evaluated at the sample level on twenty other Jonagold apples, stored and bruised under the same conditions as described in section 3a. The hypercubes for these apples were acquired at 0.1, 0.2 and 0.3 m/s to investigate the effect of the acquisition speed on the bruise detection accuracy.

3. Results and discussion

3.1. Data overview

The main parameters of the apple bruising experiment are summarized in Table 1. It can be seen that the variation in the weight of and impact energy applied to the apples was rather limited, while the variation in bruise volume was much larger. This can partially be explained by the difference in local curvature at the impact point, but can also be attributed to variability in the bruise sensitivity of the different apples.

The SWIR mean spectra using the RPM, PBR and PBARC methods for the three pixel classes (bruised, unbruised and glare) with their standard deviation are illustrated in Fig. 7. Both the PBARC and RPM calibration slightly increase the reflectance values of the spectra. Unfortunately, from the figures, the PBARC method has nearly no added value compared to PBR in this case. This similarity could originate from the fact that the observed apples are very glossy, while the reference used was 92−99% over the SWIR range. There is a higher difference in the reflectance values for the apple glare region and other regions, as shown in Fig. 7. In addition, a more significant difference between bruised and unbruised regions can be observed around the water absorption peaks at 1200, 1359 and 1658 nm (Curcio & Petty, 1951). As the bruises were scanned 2 h after bruising, they were expected to be still in the early stage of the kinetic phase of browning (Janovitz-Klapp, Richard, Goupy, & Nicolas, 1990). As the spectral changes are most apparent at the water peaks, this suggests that bruises in apples locally modify the water distribution under the skin, due to the cell rupturing by the impact. It should also be noted from Fig. 7 that the largest difference between bruised and sound tissue is between 1000 and 1800 nm, while the difference between glare and non-glare regions is also clear in the region above 1800 nm. Unfortunately, no reports with respect to the latter were found in literature (Baranowski et al., 2012; Wenqian Huang et al., 2012). It is common in hyperspectral imaging literature to consider the average spectra of apples within a multivariate model (Baranowski et al., 2012; Wenqian Huang et al., 2012). However, the fact that glossy and non-glossy regions within a same class were not separated, could explain the limitations in prior work. By averaging the spectra for unbruised (Apple), bruised (Bruise) and glossy (Glare) regions as presented in Fig. 7, glossy regions have a clearly higher reflectance above 1700 nm and a larger standard deviation across the entire spectrum than other classes.

3.2. Pixel classification

Due to the large number of combinations of methods tested, the discussion of the results in this section will be restrained to different reflectance calibration models for best performing pre-

Table 2
Summary results for binary bruise versus sound pixel-based PLS-DA bruise prediction using mean centering for different calibration methods.

Calibration method	LVs	Sensitivity	Specificity	Accuracy
RPM	9	0.871	0.86	86.27
PBR	9	0.868	0.88	88.72
PBARC	9	0.872	0.88	88.24

Table 3
Bruise prediction results for 3 class sound versus bruise versus glare pixel-based PLS-DA classifier using the first derivative with mean centering for different calibration methods.

Class	Calibration method	LVs	Sensitivity	Specificity	Accuracy
Bruise	RPM	11	0.76	0.93	92.3
	PBR	11	0.77	0.95	94.3
	PBARC	11	0.76	0.95	94.2

processing techniques, and prediction accuracy for different pre-processing techniques using the best performing reflectance calibration model.

The sensitivity, specificity and accuracy for each reflectance calibration using a binary classifier with mean centering is summarized in Table 2. The PBR reflectance calibration model presented the best accuracy and sensitivity, while the PBARC was more sensitive. As for the tree class classifier with the first derivative and posterior mean centering, PBR gave the best sensitivity, specificity and accuracy, as summarized in Table 3. The PBR calibration was therefore selected for further analysis. Comparing the classifiers, the binary one is more sensitive, but less specific than the ternary classifier. As a result, the ternary classier performs 7% better than the binary one, with 94.36% accuracy. To further understand those improvements, the reflectance of each class prior to pre-processing, with mean centering and first derivative with mean centering are illustrated in Fig. 8a, b and c, respectively. Using mean centering alone removes the constant reflectance offset, but does not correct for scattering variability. First order derivation followed by mean centering removes the scattering variability quite efficiently, such that most of the apple pixels can be distinguished from glossy and bruised regions. However, some bruised pixels (green) are confused with apple (red) or glossy (blue) regions. When observing jointly the spectra processed with first derivative and mean centering Fig. 8c and the un-processed spectra in Fig. 8a, variance appears at spectral signatures at 1200, 1359, 1450 and 1658 nm in Fig. 8c, which can be related to water absorption peaks (Curcio & Petty, 1951) in Fig. 8a, while variance at 1900 nm can be observed for glossy pixels. Observing the regression coefficients in Fig. 10a, the PLS-DA classifier assigned opposite coefficients between Glare and Apple classes around 1800 nm, and for Apple and Bruise classes at the described water absorption peaks. Therefore, the water released after the bursting of cells during bruising below the skin prior to browning could explain the ability to predict those regions using SWIR HSI. The difference between coefficient values of Glare and Apple classes could be associated with biochemical compounds located in the skin and flesh, respectively (Veraverbeke et al., 2006). Further investigations using HPLC based methods would be needed to confirm this statement quantitatively. As wavelengths around

Table 1
Jonagold apple shape and weight, impact characteristics and damage volume.

Weight g	Radius of curvature mm	Impact energy J	Max force N	Bruise volume mm^3
232.3 ± 23.4	38.8 ± 9.2	0.41 ± 0.01	76.8 ± 6.9	5013.8 ± 2752.4

Table 4
Bruise detection accuracy for pixel based reflectance calibration using a ternary PLS-DA classifier for different pre-processing techniques. The accuracy is compared to a pure pixel based prediction using all the spectrum, after removing few wavebands using a reverse iPLS, and using a particle filtering as image post-processing.

| Preprocessing technique	LVs PBR, im. Proc.	Accuracy PBR	LVs reverse iPLS	Accuracy reverse iPLS	Accuracy im. Proc.
None	12	92.3	15	91.4	94.0
1st derivative	10	93.5	14	91.7	95.6
2nd derivative	8	86.5	13	92.0	88.7
MSC (mean)	11	93.9	14	91.6	49.8
SNV	9	89.0	13	93.5	87.9
Mean Center	11	94.0	13	93.9	95.6
Normalize	11	92.4	12	92.5	93.4
1st deriv. + MC	11	94.3	16	94.3	96.2
2nd deriv. + MC	10	91.9	12	90.9	93.9
MSC + MC	10	37.1	16	93.9	93.9
SNV + MC	11	91.5	15	91.3	92.9
Normalize + MC	11	93	15	92.9	95.1
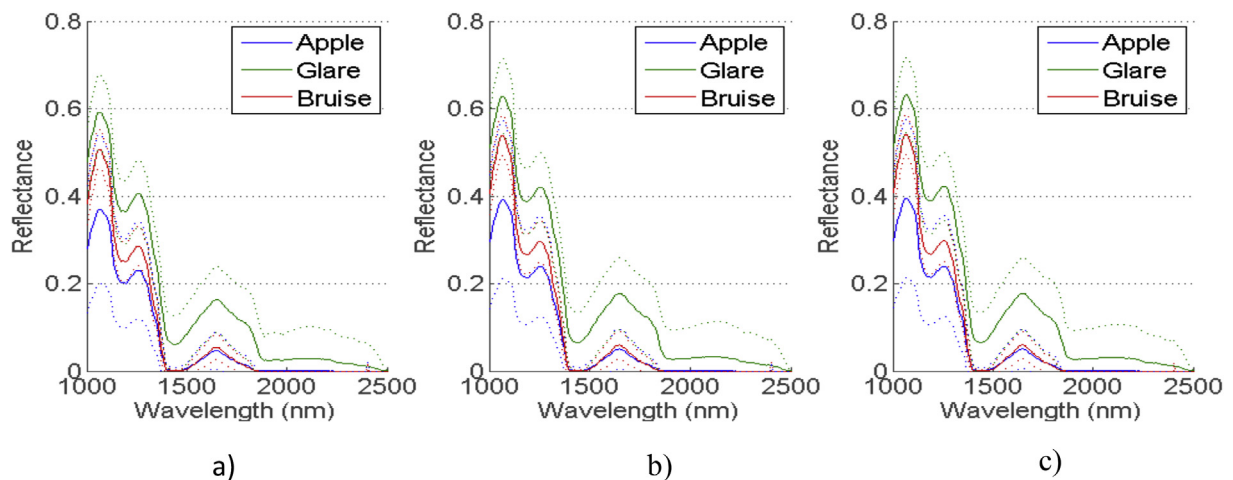
Fig. 7. Mean (solid line) +- standard deviation (dotted line) spectra acquired for apple tissue with a) traditional; b) pixel based and c) pixel based absolute reflectance calibration methods.

2450 nm and above present very low SNR, thus adding unwanted variability to the model as observed in Fig. 10c, those wavelengths were discarded during model building and prediction. To further demonstrate the contribution of PBR calibration, bruised pixel prediction using ternary PLS-DA with SR, PBR and PBARC is illustrated in Fig. 9a, b and c. The correctly classified bruised pixels are represented in green, while the ones which are in a glossy region are marked in yellow and the ones which are on a sound region in
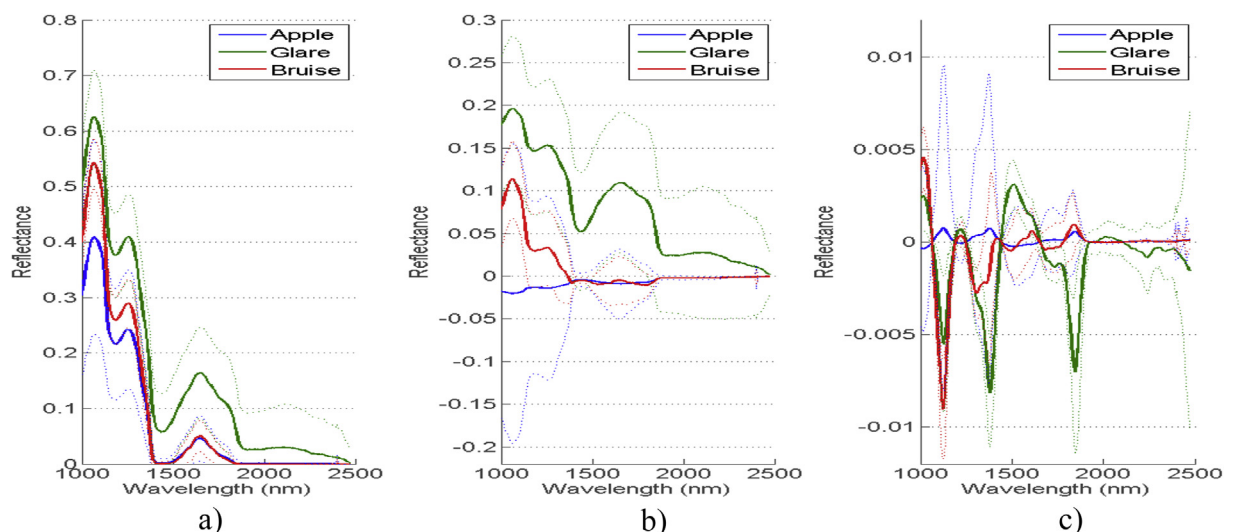
Fig. 8. Mean (solid line) +- standard deviation (dotted line) preprocessed data: a) Reflectance spectra, b) mean centering and c) 1st derivative and mean centering.
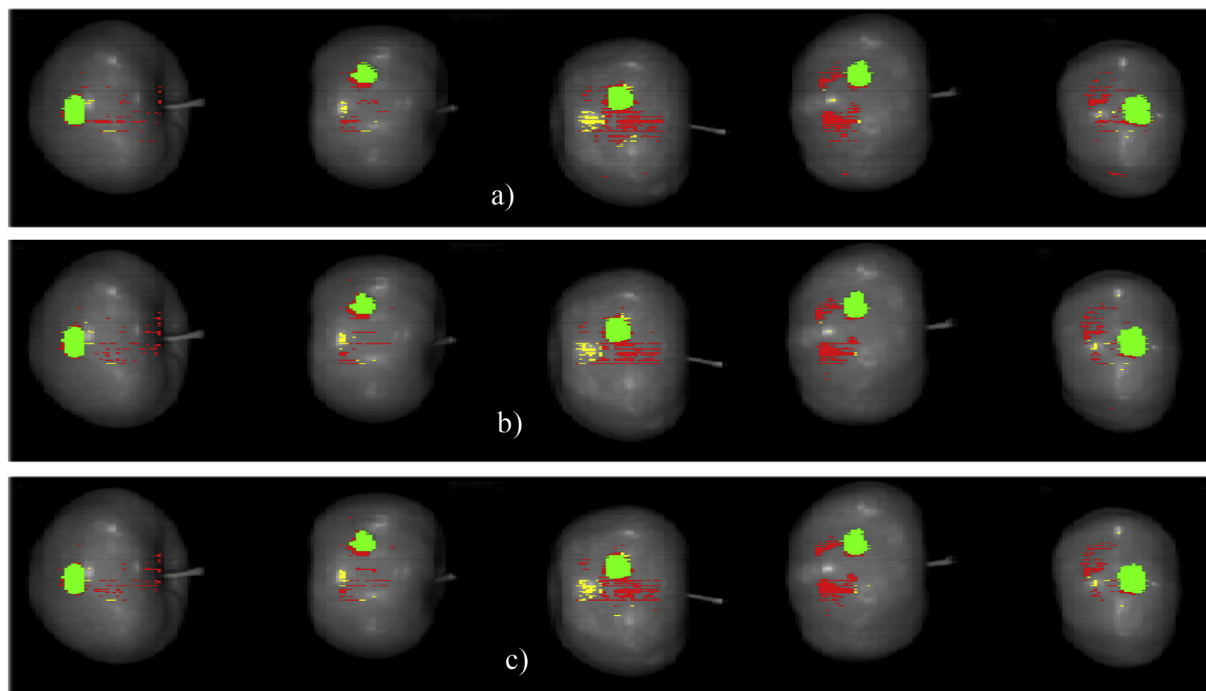
Fig. 9. Illustration of the pixel based bruise detection using a ternary PLS-DA classifier with first derivative followed by mean centering on all the spectra using a) the reference pixel method, b) pixel based reflectance and c) pixel based absolute reflectance calibration. The prediction results are superimposed on the reflectance grayscale images acquired at 1200 nm for 5 apples in the test set at 1200 nm: correctly classified bruise pixels (green), sound apple pixels predicted as bruised (red), and glare pixels (yellow). (For interpretation of the references to color in this figure legend, the reader is referred to the web version of this article.)

red. It can be observed that false positives due to pixel to pixel sensitivity variation (red and yellow) decrease when using PBR or PBARC.

3.3. Wavelength selection

In Fig. 10a, it can be observed that the best performing classifier, being the ternary PLS-DA using all wavelengths, assigned higher regression coefficient values to spectral regions associated to water absorption peaks around 1400 and 1700 nm (Curcio & Petty, 1951), which can be seen in the mean spectra (black spectrum) in Fig. 10b.

Using reverse iPLS, shorter wavebands were identified to be detrimental for the bruise detection and therefore excluded, while the longer wavelengths containing glare spectral signatures were retained as they improved bruise detection accuracy. From Table 4, it can be concluded that there is 1% improvement in the bruise detection accuracy after wavelength selection with optimal prior preprocessing.

3.4. Image post-processing

It can be seen from Table 4 that image post-processing improved
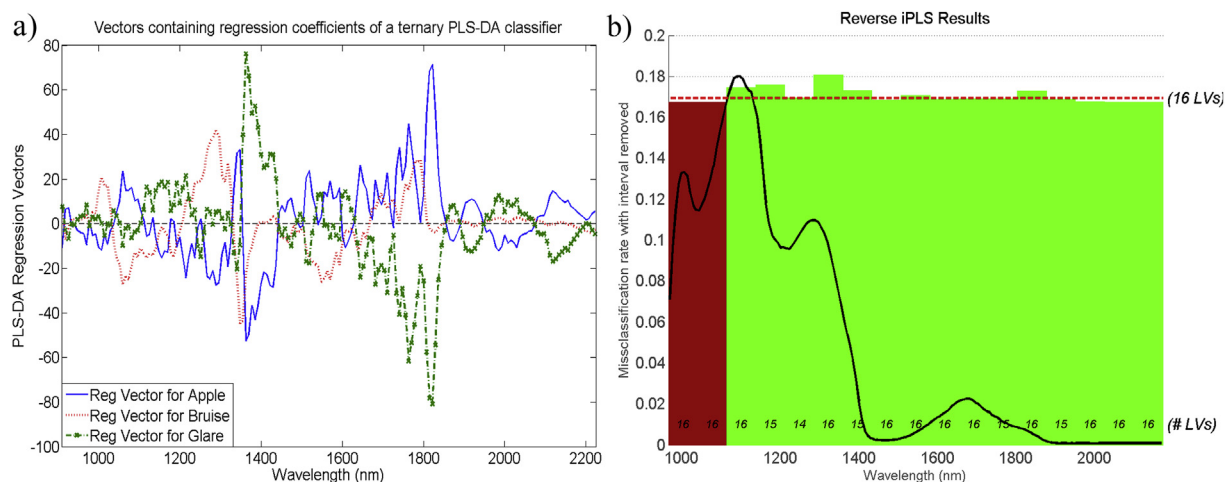
Fig. 10. Ternary PLS-DA with first derivative and mean-centering: a) regression coefficients on the latent variables using all the spectra for classes Apple, Bruise and Glare, b) automatic reverse iPLS with a spectral bandwidth of 73 nm.
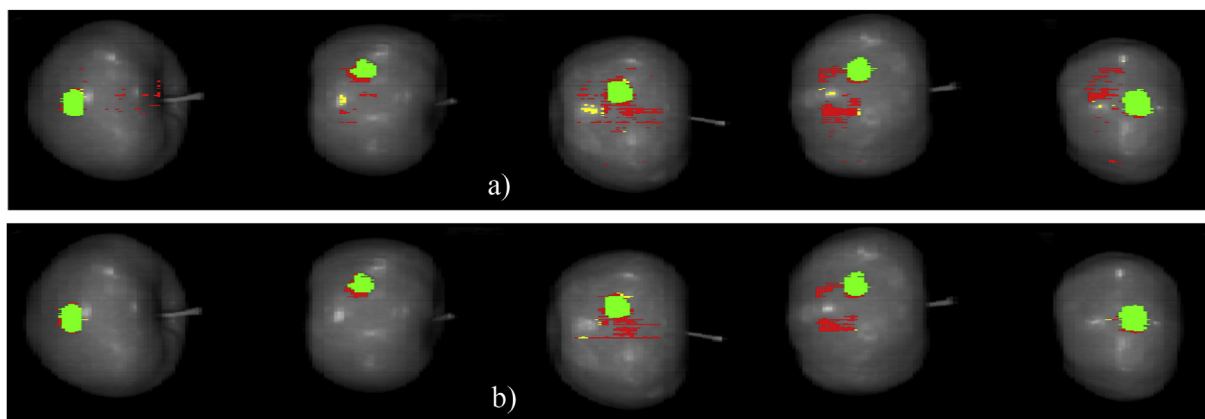
Fig. 11. Bruise prediction using a PLS-DA binary classifier with mean centering on all the spectra calibrated with PBR using a) only pixel based prediction and b) pixel based with posterior particle filtering. Using image post processing significantly reduces the false positive predictions, but some remain. The green, red and yellow pixels indicate respectively correctly predicted bruise pixels (PBP), miss-classified PBP which are sound regions, and misclassified PBP which are glossy regions. (For interpretation of the references to color in this figure legend, the reader is referred to the web version of this article.)

the prediction accuracy at the pixel level by 2% for the ternary classifiers. As a comparison, image post-processing was also applied to the best performing binary classifier using PBR with mean centering, which improved by 3% the prediction accuracy, to a value of 91.55%. The corresponding prediction images can be observed in Fig. 11 and Fig. 12, showing a clear reduction in the number of small false positive spots. However, Table 4 also points out that image post processing doesn't always improve the results, and should be used with caution. This decrease in performance is caused by the removal of too small true positive clusters as some pre-processing techniques do not always predict a clear unique convex bruised area.

3.5. Real-time validation

From Table 4, the best accuracy was obtained using the ternary PLS-DA model with 1st derivative and mean centering as pre-processing, and PBR reflectance calibration. After model loading, the bruised apples were successfully detected with 98% prediction accuracy, with an average apple processing time of 400, 300 and 200 ms for the three increasing speeds 0.1, 0.2 and 0.3 m/s. As these processing times were shorter than the average time of 600 ms needed to acquire a hypercube of an individual apple at the camera

frame rate of 60 lines per second, the data processing was fast enough for apple sorting in real-time at these conveyor speeds. A real-time demonstration can be observed in Video 1 of the sorting line for one sound followed by 3 damaged apples 2 hours after bruising at 0.1 m/s, with a closer view in Video 2. A RGB camera placed next to the SWIR HSI observed simultaneously the apples which can be seen in Video 3. Comparing videos 2 and 3, all bruises were successfully detected using SWIR HSI as it remained challenging to observe them using classical machine vision.

Supplementary data related to this article can be found at http://dx.doi.org/10.1016/j.foodcont.2016.02.007

4. Conclusions

A methodology for pixel based real-time food quality inspection using full SWIR hyperspectral imaging and optimized diffuse illumination for curved samples has been elaborated. Among the different tested reflectance calibration methods, pixel based calibration was found to reduce the sensor and improve the prediction accuracy by 2%, by reducing false positives araising from that noise. It was also shown that by applying pre-processing techniques and including glare as a separate class, using PLS-DA improved the bruise detection accuracy by 7%. This improvement could be
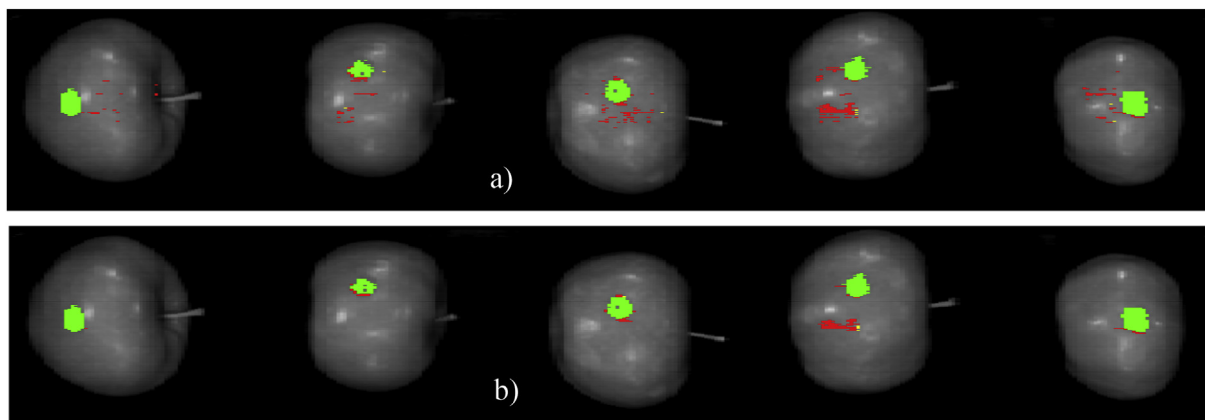
Fig. 12. Bruise prediction using a PLS-DA ternary classifier with mean centering on all the spectra calibrated with PBR using a) only pixel based prediction and b) pixel based with posterior particle filtering. Using image post processing significantly reduces the false positive predictions. The green, red and yellow pixels indicate respectively correctly predicted bruise pixels (PBP), miss-classified PBP which are sound regions, and misclassified PBP which are glossy regions. (For interpretation of the references to color in this figure legend, the reader is referred to the web version of this article.)

attributed to the inclusion of wavelengths above 1700 nm containing spectral signatures associated to those glossy regions. Considering spatial information after pixel based prediction showed an improvement of 2%. In summary, reducing unwanted variability at the sensor, glare and spatial levels gave significant improvements, resulting in a pixel-based prediction accuracy of 96.25%. However, image processing should be used with caution when detecting small defects. This study also demonstrated that pixel-based real-time SWIR hyperspectral imaging is feasible, encouraging industry to more reliable and flexible sorting solutions than current online multi-spectral techniques. While this study shows promising results for the agro-food industry, further illumination and hardware optimization is recommended to further reduce the effects of glare and to increase the processing speed, in order to promote wide application of SWIR hyperspectral imaging for rapid and non-destructive quality inspection in fruit and vegetables.

Acknowledgments

References

Ariana, D. P., & Lu, R. (2010). Evaluation of internal defect and surface color of whole pickles using hyperspectral imaging. *Journal of Food Engineering, 96*(4), 583—590.

Bae, R. N., Kim, K. W., Kim, T. C., & Lee, S. K. (2006). Anatomical observations of anthocyanin rich cells in apple skins. *HortScience, 41*(3), 733—736.

Baranowski, P., Mazurek, W., Wozniak, J., & Majewska, U. (2012). Detection of early bruises in apples using hyperspectral data and thermal imaging. *Journal of Food Engineering, 110*(3), 345—355.

Barbin, D., Elmasry, G., Sun, D.-W., & Allen, P. (2012). Near-infrared hyperspectral imaging for grading and classification of pork. *Meat Science, 90*(1), 259—268.

Battaglia, J., Burzi, V., Moyer, B., Sudol, T., & Passe, J. (2010). Parameterized nonuniformity corrections (NUC) for non-temperature stabilized InGaAs SWIR sensing. In *SPIE defense, security, and sensing (pp. 76600J—76600J)*. International Society for Optics and Photonics.

Blasco, J., Aleixos, N., & Moltó, E. (2003). Machine vision system for automatic quality grading of fruit. *Biosystems Engineering, 85*(4), 415—423.

Bollen, a. F., Nguyen, H. X., & Dela Rue, B. T. (1999). Comparison of methods for estimating the bruise volume of apples. *Journal of Agricultural Engineering Research, 74*(4), 325—330.

Cubero, S., Aleixos, N., Moltó, E., Gómez-Sanchis, J., & Blasco, J. (2011). Advances in machine vision applications for automatic inspection and quality evaluation of fruits and vegetables. *Food and Bioprocess Technology, 4*(4), 487—504.

Curcio, J., & Petty, C. (1951). The near infrared absorption spectrum of liquid water. *JOSA, 41*, 302—304.

ElMasry, G., Wang, N., Vigneault, C., Qiao, J., & ElSayed, A. (2008). Early detection of apple bruises on different background colors using hyperspectral imaging. *LWT - Food Science and Technology, 41*(2), 337—345.

Esquerre, C., Gowen, A. a, O'Donnell, C. P., & Downey, G. (2009). Initial studies on the quantitation of bruise damage and freshness in mushrooms using visible-near-infrared spectroscopy. *Journal of Agricultural and Food Chemistry, 57*(5), 1903—1907.

FAOSTAT, & F. A. O. (2016). *FAO statistical databases. Food and Agric. Organ. of the United Nations, Rome. FAOSTAT: FAO statistical databases. Food and Agric. Organ. of the United Nations, Rome.*

Feng, Y.-Z., & Sun, D.-W. (2012). Application of hyperspectral imaging in food safety inspection and control: a review. *Critical Reviews in Food Science and Nutrition, 52*(11), 1039—1058.

Goodarzi, M., & Saeys, W. (2016). Selection of the most informative near infrared spectroscopy wavebands for continuous glucose monitoring in human serum. *Talanta, 146*, 155—165.

Goodarzi, M., Sharma, S., Ramon, H., & Saeys, W. (2015). Multivariate calibration of NIR spectroscopic sensors for continuous glucose monitoring. *TrAC Trends in Analytical Chemistry, 67*, 147—158.

Horabik, J., Baranowski, P., & Tys, J. (2007). Agrophysical methods to determine bioenergetic status of agricultural products. In *11th international congress on engineering and food*.

Huang, W., Zhang, B., Li, J., & Zhang, C. (2013). Early detection of bruises on apples using near-infrared hyperspectral image. In H. Tan (Ed.), *Third international conference on photonics and image in agriculture engineering* (Vol. 8761, p. 87610P). International Society for Optics and Photonics.

Isoz, W., Svensson, T., Renhorn, I., Box, P. O., & Linköping, S.- (2005). Nonuniformity correction of infrared focal plane arrays. *Proceedings of SPIE, 5783*, 949—960.

Janovitz-Klapp, A. H. A., Richard, F. C., Goupy, P. M., & Nicolas, J. J. (1990). Kinetic studies on apple polyphenol oxidase. *Journal of Agricultural and Food Chemistry, 38*(7), 1437—1441.

Kavdir, I., & Guyer, D. E. (2005). Apple sorting using artificial neural networks and spectral imaging. *Transactions of the ASAE, 45*(6), 1995—2005.

Keresztes, J. C., De Ketelaere, B., Audenaert, J., Koshel, R. J., & Saeys, W. (2015). Illumination system development using design and analysis of computer experiments. In G. G. Gregory, A. J. Davis, & C. F. Hahlweg (Eds.), *Proc. SPIE* (Vol. 9579, p. 95790I).

Kim, M. S., Chao, K., Chan, D. E., Jun, W., Lefcourt, A. M., Delwiche, S. R. … Lee, K. (2011). Linescan hyperspectral imaging platform for agrofood safety and quality evaluation: system enhancement and characterization. *American Society of Agricultural and Biological Engineers, 54*(2), 703—711.

Kleynen, O., Leemans, V., & Destain, M.-F. (2005). Development of a multi-spectral vision system for the detection of defects on apples. *Journal of Food Engineering, 69*(1), 41—49.

Lin, M., Cavinato, A. G., Mayes, D. M., Smiley, S., Huang, Y., Al-Holy, M., et al. (2003). Bruise detection in Pacific pink salmon (Oncorhynchus gorbuscha) by visible and short-wavelength near-infrared (SW-NIR) spectroscopy (600-1100 nm). *Journal of Agricultural and Food Chemistry, 51*(22), 6404—6408.

Mehl, P. M., Chao, K., Kim, M., & Chen, Y. R. (2002). Detection of defects on selected apple cultivars using hyperspectral and multispectral image analysis. *Applied Engineering in Agriculture, 18*(2).

Mohsenin, N. N. (1984). *Physical properties of food and agricultural materials: A teaching manual.* New York Gordon and Breach Science Publishers.

Nicolaï, B. M., Beullens, K., Bobelyn, E., Peirs, A., Saeys, W., Theron, K. I., et al. (2007). Nondestructive measurement of fruit and vegetable quality by means of NIR spectroscopy: a review. *Postharvest Biology and Technology, 46*(2), 99—118.

Pang, D. W., Studman, C. J., Banks, N. H., & Baas, P. H. (1996). Rapid assessment of the susceptibility of apples to bruising. *Journal of Agricultural Engineering Research, 64*(1), 37—47.

Parra, F., Meza, P., & Torres, S. (2014). Modeling and compensating non-uniformity in push-broom NIR hyperspectral imaging system. *Infrared Physics & Technology, 63*, 204—210.

Russell, B. C., Torralba, A., Murphy, K. P., & Freeman, W. T. (2008). LabelMe: a database and web-based tool for image annotation. *International Journal of Computer Vision, 77*(1—3), 157—173.

Serranti, S., Cesare, D., & Bonifazi, G. (2013). The development of a hyperspectral imaging method for the detection of Fusarium-damaged, yellow berry and vitreous Italian durum wheat kernels. *Biosystems Engineering, 115*(1), 20—30.

Soliva-Fortuny, R. C. R., Grigelmo-Miguel, N., Odriozola-Serrano, I., Gorinstein, S., & Mart'in-Belloso, O. (2001). Browning evaluation of ready-to-eat apples as affected by modified atmosphere packaging. *Journal of Agricultural and Food Chemistry, 49*(8), 3685—3690.

Unay, D., Gosselin, B., Kleynen, O., Leemans, V., Destain, M.-F., & Debeir, O. (2011). Automatic grading of Bi-colored apples by multispectral machine vision. *Computers and Electronics in Agriculture, 75*(1), 204—212.

Van Zeebroeck, M., Tijskens, E., Liedekerke, P. V., Deli, V., Baerdemaeker, J. D., & Ramon, H. (2003). Determination of the dynamical behaviour of biological materials during impact using a pendulum device. *Journal of Sound and Vibration, 266*(3), 465—480.

Van Zeebroeck, M., Van linden, V., Ramon, H., De Baerdemaeker, J., Nicolaï, B. M., & Tijskens, E. (2007). Impact damage of apples during transport and handling. *Postharvest Biology and Technology, 45*(2), 157—167.

Veraverbeke, E. a., Verboven, P., Lammertyn, J., Cronje, P., De Baerdemaeker, J., & Nicolaï, B. M. (2006). Thermographic surface quality evaluation of apple. *Journal of Food Engineering, 77*(1), 162—168.

VLAM.. (2015). *Vlaams Centrum voor Agro- en Visserijmarketing.*

Wenqian, H., Zhang, C., Li, J., Chen, L., & Zhao, C. (2012). Detection of bruise and stem-end/calyx of apples using hyperspectral imaging and segmented principal component analysis. In *ASABE annual international meeting* (Vol. 7004)St. Joseph, MI: American Society of Agricultural and Biological Engineers.

Wen, Z., & Tao, Y. (1999). Building a rule-based machine-vision system for defect inspection on apple sorting and packing lines. *Expert Systems with Applications, 16*(3), 307—313.

Wu, D., Shi, H., Wang, S., He, Y., Bao, Y., & Liu, K. (2012). Rapid prediction of moisture content of dehydrated prawns using online hyperspectral imaging system. *Analytica Chimica Acta, 726*, 57—66.

Xing, J., Symons, S., Hatcher, D., & Shahin, M. (2011). Comparison of short-wavelength infrared (SWIR) hyperspectral imaging system with an FT-NIR spectrophotometer for predicting alpha-amylase activities in individual Canadian Western Red Spring (CWRS) wheat kernels. *Biosystems Engineering, 108*(4), 303—310.

Zarifneshat, S., Ghassemzadeh, H. R., Sadeghi, M., Abbaspour-Fard, M., Hossein, A. E., Javadi, A., et al. (2010). Effect of impact level and fruit properties on golden delicious apple bruising. *American Journal of Agricultural and Biological Science, 5*(2), 114—121.